AJ; submitted 2015 March 18; accepted 2015 December 18
Preprint typeset using LaTeX style emulateapj v. 5/2/11

FAST, LOW-IONIZATION EMISSION REGIONS OF THE PLANETARY NEBULA M2-42

A. Danehkar[1,2], Q. A. Parker[1,3,4], and W. Steffen[5]

AJ; submitted 2015 March 18; accepted 2015 December 18

ABSTRACT

Spatially resolved observations of the planetary nebula M2-42 (PN G008.2−04.8) obtained with the Wide Field Spectrograph on the Australian National University 2.3 m telescope have revealed the remarkable features of bipolar collimated jets emerging from its main structure. Velocity-resolved channel maps derived from the [N II] λ6584 emission line disentangle different morphological components of the nebula. This information is used to develop a three-dimensional morpho-kinematic model, which consists of an equatorial dense torus and a pair of asymmetric bipolar outflows. The expansion velocity of about 20 $\mathrm{km\,s^{-1}}$ is measured from the spectrum integrated over the main shell. However, the deprojected velocities of the jets are found to be in the range of 80–160 $\mathrm{km\,s^{-1}}$ with respect to the nebular center. It is found that the mean density of the collimated outflows, $595 \pm 125\,\mathrm{cm^{-3}}$, is five times lower than that of the main shell, $3150\,\mathrm{cm^{-3}}$, whereas their singly ionized nitrogen and sulfur abundances are about three times higher than those determined from the dense shell. The results indicate that the features of the collimated jets are typical of fast, low-ionization emission regions.

Subject headings: ISM: jets and outflows – planetary nebulae: individual (M2-42) – stars: evolution

1. INTRODUCTION

M2-42 (= PN G008.2−04.8 = Hen 2-393 = VV 177 = Sa 2-331) was discovered as a planetary nebula (PN) by Minkowski (1947). The Hα image, Fig. 1 (top panel), obtained from the AAO/UKST SuperCOSMOS Hα Sky Survey (SHS; Parker et al. 2005) revealed an elliptical morphological structure with a clear extension to the north east, suggesting the presence of bipolar outflows. The long-slit data from the San Pedro Mártir kinematic catalog (SPM; López et al. 2012) disclosed the presence of a dense torus-like component and collimated bipolar outflows (Akras & López 2012). The JHK_s image, Fig. 1 (bottom panel), obtained from the VISTA variables in the Vía Láctea Survey (VVV; Saito et al. 2012) also shows the presence of a compact dusty torus embedded in the main shell.

Wang & Liu (2007) carried out plasma diagnostics and abundance analysis of M2-42 using deep long-slit optical spectroscopy. They derived a mean electron density of $N_\mathrm{e} \simeq 3 \times 10^3\,\mathrm{cm^{-3}}$, and an electron temperature of $T_\mathrm{e} = 9\,350$ K from the [N II] line ratio, which is consistent with those of other PNe (see e.g. Kingsburgh & Barlow 1994). The oxygen abundance of O/H = 5.62×10^{-4} derived by Wang & Liu (2007) is slightly above the solar metallicity, while N/O = 0.32 corresponds to a non-Type I PN (based on N/O < 0.8; Kingsburgh & Barlow 1994).

The central star of M2-42 depicts weak emission-line star characteristics (*wels* defined by Tylenda et al. 1993) dominated by nitrogen and helium (DePew et al. 2011). The nebular spectrum of moderate excitation, $I(5007) = 807$ on a scale where $I(\mathrm{H}\beta) = 100$ (Wang & Liu 2007), is related to an excitation class of 3.6 (Dopita & Meatheringham 1990), and a stellar temperature of 74 kK (Dopita & Meatheringham 1991) or 69 kK (Reid & Parker 2010). Based on the Energy-Balance method, Preite-Martinez et al. (1989) estimated a stellar temperature of 74.9 kK. According to Tylenda et al. (1991a), the central star has a B magnitude of 18.2. Using the H I Zanstra method, Tylenda et al. (1991b) derived a stellar temperature of 56 kK and a luminosity of $\log L/\mathrm{L}_\odot = 2.87$, which correspond to a current core mass of $0.62\mathrm{M}_\odot$.

Based on its angular diameter and radio brightness (6 cm), Acker et al. (1991) suggested that M2-42 is most likely located in the Galactic bulge. Cahn et al. (1992) estimated a distance of 8754 pc to the PN, which places it near to the Galactic center. The most recent distance estimation by Stanghellini et al. (2008) yielded a distance of 9444 pc. Moreover, we estimate a distance of 7400^{+570}_{-550} from the Hα surface brightness-radius relation for a sample of 332 PNe (Frew et al. 2016), total flux value of $\log F(\mathrm{H}\alpha) = -11.39$ $\mathrm{erg\,cm^{-2}\,s^{-1}}$ (Frew et al. 2013), $c(\mathrm{H}\beta) = 0.99$ (Wang & Liu 2007), and angular radius of 2 arcsec (Stanghellini et al. 2008). Therefore, it could be a Galactic Bulge PN (GBPN).

In this paper, we present our integral field spectroscopy of M2-42, from which we determine ionization and kinematic properties of the nebula and its collimated outflows. In Section 2, we present the observations together with the physical and chemical conditions, stellar characteristics, and kinematic results derived from our data. Section 3 describes the morpho-kinematic model of M2-42 and, finally, in Section 4 we draw our conclusion.

ashkbiz.danehkar@cfa.harvard.edu
[1] Department of Physics and Astronomy, Macquarie University, Sydney, NSW 2109, Australia
[2] Harvard-Smithsonian Center for Astrophysics, 60 Garden Street, Cambridge, MA 02138, USA
[3] Australian Astronomical Observatory, P.O. Box 915, North Ryde, NSW 1670, Australia
[4] Department of Physics, The University of Hong Kong, Pokfulam Road, Hong Kong, China
[5] Instituto de Astronomía, Universidad Nacional Autónoma de México, C.P.22860, Ensenada, Mexico

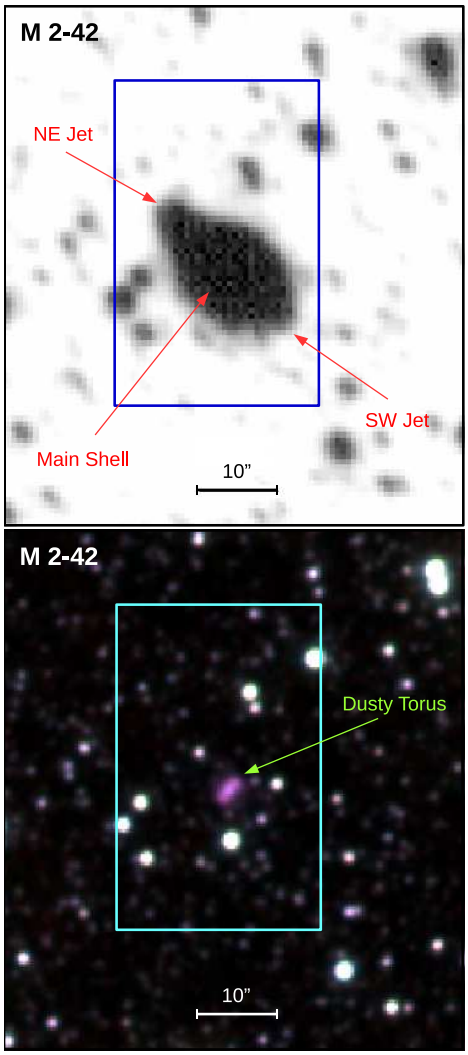

Figure 1. Top panel: the Hα image obtained from the SHS (Parker et al. 2005) with the morphological features labeled. The rectangle shows the $25'' \times 38''$ WiFeS field of view observed using the ANU 2.3-m telescope in 2010 April. The image scale is shown by a solid line. North is up and east is toward the left-hand side. Bottom panel: the JHK_s image obtained from the VVV Survey (Saito et al. 2012) with the compact dusty torus labeled. The red, green, and blue colors are assigned to the K_s, H, and J, respectively.

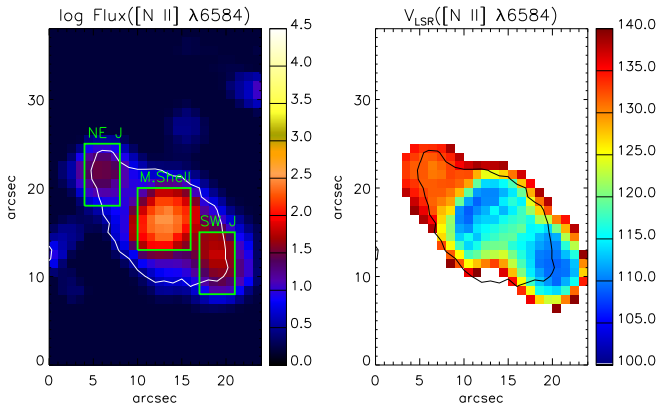

Figure 2. From left to right, spatial distribution maps of flux intensity and LSR velocity of [N II] λ6584. Flux unit is in logarithm of 10^{-15} erg s^{-1} cm^{-2} spaxel^{-1} and velocity in km s^{-1}. The rectangles show apertures used to extract fluxes across the main shell ($6'' \times 7''$), and the NE and SW jets ($4'' \times 7''$). The white/black contour lines show the distribution of the narrow-band emission of Hα in arbitrary unit obtained from the SHS. North is up and east is toward the left-hand side.

2. OBSERVATIONS

Moderate resolution, integral field observations were obtained on 2010 April 22 under program number 1100147 (PI: Q. A. Parker) with the Wide Field Spectrograph (WiFeS; Dopita et al. 2007, 2010) mounted on the Australian National University (ANU) 2.3 m telescope at Siding Spring Observatory. CCD chips with 4096 × 4096 pixels are used as detectors. The spectrograph samples $0\farcs5$ along each of twenty five $38'' \times 1''$ slitlets, which provides a field of view of $25'' \times 38''$ and a spatial resolution element of $1\farcs0 \times 0\farcs5$. Each slitlet is designed to project to 2 pixels on the CCD chips, yielding a reconstructed point-spread function with a full width at half maximum (FWHM) of $\sim 2''$.

Figure 1 shows the WiFeS areal footprint used for our study. The main shell, the northeast (NE) jet and the southwest (SW) jet are also labeled on the figure. We used the spectral resolution of $R \sim 7000$, covering $\lambda\lambda$4415–5589 Å in the blue channel and $\lambda\lambda$5222–7070 Å in the red channel. The red spectrum has a linear wavelength dispersion per pixel of 0.45 Å, which yields a resolution of ~ 20 km s^{-1} in velocity channels. The exposure time of 20 minutes used for our observation yields a signal-to-noise ratio of S/N $\gtrsim 10$ for the [N II] emission line. Data reduction was performed with the wifes IRAF package (described by Danehkar et al. 2013, 2014).

Table 1 presents a full list of observed line fluxes measured from three different apertures shown in Fig. 2: the main shell ($6'' \times 7''$), the NE jet ($4'' \times 7''$) and the SW jet ($4'' \times 7''$). The laboratory wavelength, emission line identification and multiplet number are given in columns 1–3, respectively. Columns 4–9 present the observed line fluxes $F(\lambda)$ and the dereddened fluxes $I(\lambda)$ after correction for interstellar extinction for the three different regions, respectively. All fluxes are given relative to Hβ, on a scale where Hβ = 100. To extract the observed line fluxes, we applied a single Gaussian profile to each line. The logarithmic extinction c(Hβ) was calculated from the Balmer flux ratio Hα/Hβ. However, we adopted the extinction c(Hβ)= 0.989 derived by Wang & Liu (2007) for the main shell since the Hα emission line was saturated over the main shell area.

2.1. *Physical and chemical conditions*

Electron temperature T_e and electron density N_e for the different regions of M2-42 are presented in Table 2. The electron temperatures and densities were obtained using the EQUIB code (Howarth & Adams 1981) from the [N II] nebular to auroral line ratio and the [S II] doublet line ratio, respectively. The electron temperature $T_e([\mathrm{N\,II}])_{\mathrm{corr}}$ was corrected for recombination contribution to the auroral line using the formula given by Liu et al. (2000) and the ionic abundance N^{++}/H^+ derived from the N II lines. The values of $N_e([\mathrm{S\,II}]) = 3150\,\mathrm{cm}^{-3}$ and $T_e([\mathrm{N\,II}])_{\mathrm{corr}} = 9600\,\mathrm{K}$ are in agreement with $N_e([\mathrm{S\,II}]) = 3240\,\mathrm{cm}^{-3}$

Table 1
Observed line fluxes $F(\lambda)$ and dereddened fluxes $I(\lambda)$ measured from the apertures shown in Fig. 2.

λ_0(Å)	ID	Mult	Main Shell		NE Jet		SW Jet	
			$F(\lambda)$	$I(\lambda)$	$F(\lambda)$	$I(\lambda)$	$F(\lambda)$	$I(\lambda)$
4471.50	He I	V14	4.56	5.67	4.07	4.97	3.75	4.58
4609.44	O II	V92a	0.03	0.04	–	–	–	–
4634.14	N III	V2	0.13	0.15	–	–	–	–
4649.13	O II	V1	0.35	0.39	–	–	–	–
4676.23	O II	V1	0.09	0.10	–	–	–	–
4685.68	He II	3.4	0.30	0.34	0.34	0.37	–	–
4740.17	[Ar IV]	F1	0.51	0.54	–	–	–	–
4861.33	H I 4-2	H4	100.00	100.00	100.00	100.00	100.00	100.00
4881.11	[Fe III]	F2	0.05	0.05	–	–	–	–
4921.93	He I	V48	1.45	1.41	–	–	1.68	1.63
4958.91	[O III]	F1	226.94	214.89	172.83	164.37	193.45	184.01
5006.84	[O III]	F1	728.99	672.08	529.92	491.74	589.62	547.27
5666.63	N II	V3	0.07	0.04	–	–	–	–
5679.56	N II	V3	0.11	0.07	–	–	–	–
5754.60	[N II]	F3	1.03	0.66	2.21	1.47	1.35	0.90
5875.66	He I	V11	24.78	15.20	23.82	15.20	25.96	16.58
6101.83	[K IV]	F1	0.05	0.03	–	–	–	–
6312.10	[S III]	F3	2.24	1.18	–	–	–	–
6461.95	C II	V17.04	0.12	0.06	–	–	–	–
6548.10	[N II]	F1	26.55	12.87	82.73	42.49	56.74	29.21
6562.77	H I 3-2	H3	–	286.00	564.29	288.58	564.65	289.38
6583.50	[N II]	F1	81.59	39.10	258.01	131.14	174.03	88.64
6678.16	He I	V46	8.60	4.00	8.59	4.25	8.81	4.36
6716.44	[S II]	F2	8.16	3.75	39.09	19.11	28.82	14.12
6730.82	[S II]	F2	12.97	5.93	36.51	17.78	30.02	14.65
$c(\mathrm{H}\beta)$				0.989		0.910		0.907

and $T_e([\mathrm{N\,II}]) = 9350\,\mathrm{K}$ derived by Wang & Liu (2007). Additionally, we determined the physical conditions of the NE and SW jets. The jets show a mean electron temperature of $8840 \pm 180\,\mathrm{K}$, which is 760 K lower than that of the main shell, whereas their mean electron density of $595 \pm 125\,\mathrm{cm}^{-3}$ is by a factor of five lower than that of the main shell.

Table 2 also lists the ionic abundances X^{i+}/H^+ derived from collisionally excited lines (CELs) and optical recombination lines (ORLs). We used the EQUIB code to calculate the ionic abundances. We adopted the physical conditions, T_e ($T_{e\,corr}$ for the main shell) and N_e, derived from CELs. The atomic data sets used for plasma diagnostics and abundances analysis are the same as those used by Danehkar (2014, Chapter 3).

Our value of $He^+/H^+ = 0.105$ for the main shell is in good agreement with $He^+/H^+ = 0.107$ derived by Wang & Liu (2007). However, they derived $O^{++}/H^+ = 5.27 \times 10^{-4}$, which is twice our value. This could be due to the different atomic data used by them. Our values of N^+/H^+, S^+/H^+ and Ar^{3+}/H^+ are in reasonable agreement with $N^+/H^+ = 1.03 \times 10^{-4}$, $S^+/H^+ = 4.96 \times 10^{-7}$ and $Ar^{3+}/H^+ = 1.59 \times 10^{-7}$ obtained by Wang & Liu (2007). Note that a slit with a width of $2''$ used by Wang & Liu (2007) is not completely related to the main shell. We see that the abundance discrepancy factor for O^{++}, $\mathrm{ADF}(O^{++}) \equiv (O^{++}/H^+)_{ORL}/(O^{++}/H^+)_{CEL} = 3.14$, is in agreement with $\mathrm{ADF}(O^{++}) = 2.09$ (Wang & Liu 2007). Moreover, our abundance ratio of $(N^{++}/O^{++})_{ORL} = 0.388$ derived from ORLs is in excellent agreement with $(N^{++}/O^{++})_{ORL} = 0.399$ obtained by Wang & Liu (2007). Although He^+/H^+ and O^{++}/H^+ derived from the jets are similar to those of the main shell, N^+/H^+ and S^+/H^+ derived from the jets are about three times higher than those of the main shell. These ionization features of the bipolar collimated jets are typical of fast, low-ionization emission regions (FLIERs; Balick et al. 1993, 1994, 1998).

Table 2
Electron temperature T_e, electron density N_e and ionic abundances derived from the dereddened fluxes listed in Table 1.

Parameter	Main Shell	NE Jet	SW Jet
$T_e([\mathrm{N\,II}])(\mathrm{K})$	10270	9020	8660
$T_e([\mathrm{N\,II}])_{corr}(\mathrm{K})$	9600	–	–
$N_e([\mathrm{S\,II}])(\mathrm{cm}^{-3})$	3150	470	720
$(He^+/H^+)_{ORL}$	0.105	0.107	0.110
$(N^+/H^+)_{CEL} \times 10^5$	0.764	2.912	2.236
$(O^{++}/H^+)_{CEL} \times 10^4$	2.606	2.469	3.208
$(S^+/H^+)_{CEL} \times 10^6$	0.347	1.150	1.040
$(S^{++}/H^+)_{CEL} \times 10^6$	3.116	–	–
$(Ar^{3+}/H^+)_{CEL} \times 10^7$	1.871	–	–
$(N^{++}/H^+)_{ORL} \times 10^4$	3.175	–	–
$(O^{++}/H^+)_{ORL} \times 10^4$	8.185	–	–

2.2. *Comments on stellar characteristics*

The stellar emission-line fluxes presented in Table 3, are measured from a spectrum integrated over an

Table 3
Stellar emission-line fluxes $I(\lambda)$ on a scale where C IV 5805 = 100, equivalent width W_λ(Å), and FWHM (Å).

Line	λ(Å)	$I(\lambda)$	W_λ(Å)	FWHM(Å)
N V	4603	33.58:	−1.16	3.14
N III	4634	77.56	−3.15	1.25
N III	4641	283.41	−10.91	3.08
C III/IV	4650	220.38	−9.49	2.97
C III	4655	42.05	−1.94	3.55
C IV	4659	63.19	−2.81	2.84
He II	4686	139.46	−8.17	1.23
N V	4932	57.20:	−2.93	2.47
C IV	5805	100.00	−5.62	10.27
C II	6462	19.28	−1.11	2.09
C III	7037	16.29:	−1.04	5.01

aperture ($3'' \times 3''$) covering the central star in the WiFeS field. The emission line identification, wavelength, dereddened flux corrected for reddening using $c(\mathrm{H}\beta)$= 0.99, equivalent width W_λ (Å), and FWHM (Å) are given in columns 1–5, respectively. All fluxes are given relative to C IV 5805, on a scale where C IV 5805 = 100. We note that the width of C IV λ5805 is narrower than typical Wolf–Rayet central starts of PNe with the same stellar temperature (see e.g., Crowther et al. 1998; Acker & Neiner 2003), so it could be a *wels* as identified by DePew et al. (2011). Following the method used by Acker & Neiner (2003), a terminal wind velocity of 640 km s^{-1} is deduced from FWHM(C IV λ5805) = 10.27 Å. However, we get a terminal velocity of 1560 km s^{-1} from FWHM(C IV λ5805) = 25 Å reported by DePew et al. (2011). Although the C III λ5696 line is not detected, the C III/IV λ4650 is possibly identified. The He II λ4686 line is fairly strong, but it could have a nebular origin. We see the presence of strong N III $\lambda\lambda$4634,4641 lines and weak N V $\lambda\lambda$4603,4932 lines. Assuming that the He II λ4686 line is a stellar emission line, M2-42 could have a stellar characteristics similar to WN8-type stars of van der Hucht (2001) based on I(N III λ4641) $\gtrsim$ I(He II λ4686) and I(N III) $\gg$ I(N V). However, N II λ3995 and N IV $\lambda\lambda$3479–3484, 4058 lines are not in the wavelength coverage of our WiFeS observations, so we cannot certainly classify it as one of nitrogen sequences of Wolf–Rayet central stars of PNe.

2.3. *Kinematic results*

We derived an expansion velocity of V_{HWHM} = 20.2 ± 1.3 km s^{-1} from the half width at half maximum (HWHM) for the [N II] $\lambda\lambda$6548,6584 and [S II] $\lambda\lambda$6716,6731 emission-line profiles integrated over the main shell ($6'' \times 7''$). The local standard of rest (LSR) systemic velocity of the whole nebula was estimated to be at 122.9 ± 12 km s^{-1}, which is in agreement with V_{LSR} = 133.1 ± 13.3 km s^{-1} measured by Durand et al. (1998). The LSR velocity is defined as the line of sight radial velocity, transferred to the local standard of rest by correcting for the motions of the Earth and Sun.

Figure 2 shows spatially resolved flux and velocity maps of M2-42 extracted from the [N II] λ6584 emission line across the WiFeS field. The observed radial velocity

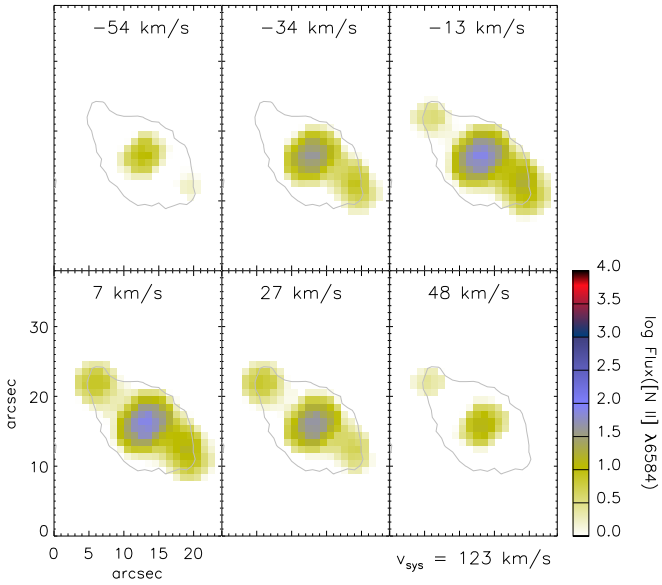

Figure 3. Velocity slices of M2-42 along the [N II] λ6584 emission-line profiles. The slices have a $\sim$ 20 km s^{-1} width, the central velocity is given at the top of each slice, and the LSR systemic velocity is v_{sys} = 123 km s^{-1}. The color bars show flux measurements in logarithm of 10^{-15} erg s^{-1} cm^{-2} spaxel^{-1}. Velocity channels are in km s^{-1}. The contours in the channel maps are the narrow-band Hα emission in arbitrary unit obtained from the SHS. North is up and east is toward the left-hand side.

map was transferred to the LSR radial velocity. The white/black contour lines in the figures depict the 2D distribution of the Hα emission obtained from the SHS, which can aid us in distinguishing the nebular border. As seen in Fig. 2, the kinematic map depicts an elliptical structure with a pair of collimated bipolar outflows, which is easily noticeable in the channel maps (see Fig. 3) and discussed below.

Figure 3 presents the flux intensity maps of the [N II] λ6584 emission lines on a logarithmic scale observed in a sequence of 6 velocity channels with a resolution of $\sim$ 20 km s^{-1}, which can be used to identify different morphological components of the nebula. We subtracted the systemic velocity v_{sys} = 123 km s^{-1} from the central velocity value given at the top of each channel. The stellar continuum map was also subtracted from the flux intensity maps. While there is a dense torus in the center, a pair of collimated bipolar outflows can be also identified in the velocity channels. The torus has a radius of $3'' \pm 1''$. This torus is clearly evident in the VVV J, H, and K_{s} color combined image of M2-42 presented in Figure. 1 (bottom panel). We notice that the bipolar outflows are highly asymmetric, the SW jet apparently having a bow shock structure. While the NE jet reaches a distance of $12'' \pm 2''$ from the nebular center, the distance of the SW jet from the central star is about 25% shorter than the NE jet. Interaction with the interstellar medium (ISM) can lead to the formation of asymmetric bipolar outflows (see e.g. Wareing et al. 2007). Both the jet components have similar brightness in the velocity channels. Brightness discontinuities are seen in the channels, where the bipolar outflows emerge from the main shell.

Table 4
Parameters of the Morpho-kinematic model of M2-42.

Parameter	Value
Inclination of major axis, i	$-82° \pm 4°$
Position angle of major axis, PA	$50° \pm 5°$
Galactic position angle of major axis, GPA	$112°24' \pm 5°$
Outer radius of the main shell	3 ± 1 arcsec
NE Jet distance from the center	12 ± 2 arcsec
SW Jet distance from the center	9 ± 2 arcsec
Jet velocity from the center	120 ± 40 km s^{-1}

3. MORPHO-KINEMATIC MODEL

We have used the morpho-kinematic modeling program SHAPE (version 5.0) described in detail by Steffen & López (2006) and Steffen et al. (2011). This program has been used for modeling many PNe, such as NGC 2392 (García-Díaz et al. 2012), NGC 3242 (Gómez-Muñoz et al. 2015), Hen 2-113 and Hen 3-1333 (Danehkar & Parker 2015). It uses interactively molded geometrical polygon meshes to generate three-dimensional structures of gaseous nebulae. The program produces several outputs that can be directly compared with observations, namely position-velocity diagrams, velocity channels and synthetic images. The modeling procedure consists of defining the geometry, assigning a density distribution and defining a velocity law. Geometrical and kinematic parameters are modified in a manual interactive process until a satisfactorily fitting model has been constructed.

Figure 4 (a) shows the morpho-kinematic model before rendering at two different orientations (inclination: 0° and 90°), and their best-fitting inclination, together with the result of the rendered model. The morpho-kinematic model consists of an equatorial dense torus (main shell) and a pair of asymmetric bipolar outflows. The values of the parameters of the final model are summarized in Table 4. For the velocity field, we assume a Hubble-type flow (Steffen et al. 2009).

The velocity-channel maps of the final model are shown in Figure 4 (b), where they can be directly compared with the observed velocity-resolved channel maps presented in Figure 3. The model maps are a good match to the observational maps. The model successfully produces two kinematic components of the jets moving in opposite directions on both sides of the torus. From the morpho-kinematic model, we derived an inclination of $i = -82° \pm 4°$ with respect to the line of sight. Taking the inclination derived by the best-fitting model, we estimated a "jet" expansion velocity of 120 ± 40 km s^{-1} with respect to the central star.

As seen in Table 4, the symmetric axis of the bipolar outflows has a position angle (PA) of $50° \pm 5°$ measured from the north toward the east in the equatorial coordinate system (ECS). This leads to a Galactic position angle (GPA) of 112.°4. The GPA is the position angle of the nebular symmetric axis projected on to the sky plane, measured from the North Galactic Pole toward the Galactic east. Note that GPA = 90° describes an alignment with the Galactic plane,

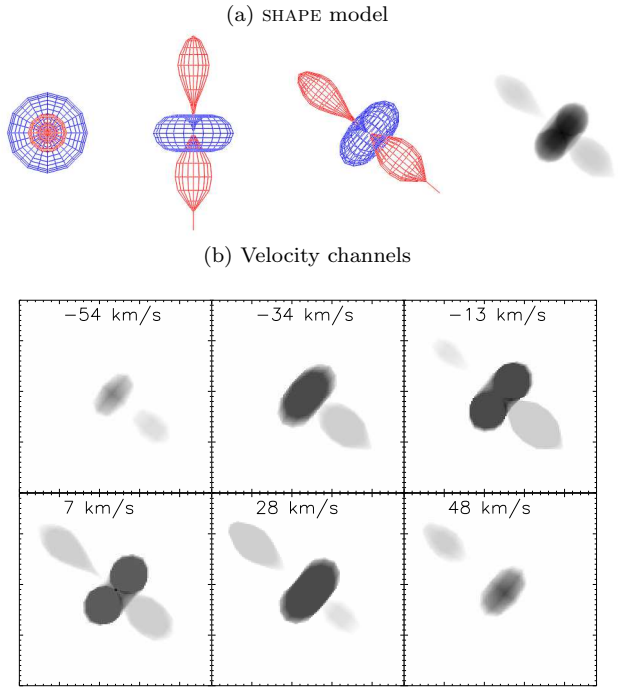

Figure 4. Top panels: SHAPE mesh model of M2-42 before rendering at two different orientations (inclination: 0° and 90°), the best-fitting inclination, and the corresponding rendered image, respectively. Bottom panels: synthetic images at different velocity channels obtained from the best-fitting SHAPE model.

whereas GPA = 0° is perpendicular to the Galactic plane. Therefore, the symmetric axis of M2-42 is roughly aligned with the Galactic plane. This alignment could have some implications for other studies of GBPNe (see e.g. Rees & Zijlstra 2013; Falceta-Gonçalves & Monteiro 2014; Danehkar & Parker 2016).

4. SUMMARY AND DISCUSSIONS

In this paper, we present the spatially resolved observations of M2-42 obtained with the WiFeS on the ANU 2.3 m telescope. Using the velocity-resolved channel maps derived from the [N II] λ6584 emission line, a morpho-kinematic model has been developed which includes different morphological components of the nebula: a dense torus and a pair of asymmetric bipolar outflows in opposite directions. From the HWHM method, the torus is found to expand slowly at 20 km s^{-1}, almost in agreement with 15 km s^{-1} derived by Akras & López (2012). From the reconstruction model, the trail of bipolar outflows was found to go along the direction of (GPA, i) = (112°, −82°), which is very similar to the inclination of $i = 77°$ derived by Akras & López (2012) based on the SPM long-slit data. We find a "jet" expansion velocity of 120 ± 40 km s^{-1} with respect to the nebular center, which is higher than the value of 70 km s^{-1} estimated by Akras & López (2012). Moreover, we found that the SW jet, which moves toward us, has possibly a bow shock structure relating to the interaction with ISM (see e.g. Wareing et al. 2007).

An empirical analysis of the nebular spectra separately integrated over the three different regions shows that the mean density of the jets is a factor of five lower than that

in the main shell. Although the abundances of singly ionized helium and doubly ionized oxygen are almost the same in both the shell and the jets, the singly ionized nitrogen and sulfur abundances derived from the jets are about three times higher than those obtained from the main shell. The similar ionization characteristics have been found in collimated jets emerged from other PNe (see e.g. Balick et al. 1993, 1994).

Nearly 10% of Galactic PNe have been found to have the small-scale low-ionization structures in opposite directions on both sides of their central stars. Around half of them are fast, highly collimated outflows with velocities of 30–200 $\mathrm{km\,s^{-1}}$ relative to the main bodies, so called FLIERs (Balick et al. 1993, 1994, 1998). Previously, Balick et al. (1994) claimed the presence of nitrogen enrichment by factors of 2–5 in the FLIERs of some PNe. However, Gonçalves et al. (2003) suggested that empirically derived nitrogen overabundance seen in FLIERs are a result of inaccurate ionization correction factors applied in the empirical analysis. Gonçalves et al. (2006) constructed a chemically homogeneous photoionization model of NGC 7009, which can reproduce the ionization characteristics of its shell and FLIERs. Similarly, the enhancement of N^+/H^+ and S^+/H^+ in the FLIERs of M2-42 could be attributed to the geometry and density distribution rather than chemical inhomogeneities.

The previous observations of M2-42 showed that its central star is of *wels* type (DePew et al. 2011). Moreover, we found that its stellar spectrum might be similar to the WN8 subclass of van der Hucht (2001) based on $I(\mathrm{N\,III}) \gtrsim I(\mathrm{He\,II})$. The terminal wind velocity was also estimated to be about 640 $\mathrm{km\,s^{-1}}$. However, our observations did not cover the N II and N IV lines, which are necessary for the WN classification. This typical stellar characteristics and its point-symmetric morphology could be a result of a common-envelope evolutionary phase (see e.g. Nordhaus & Blackman 2006). Currently, there is no evidence for binarity in M2-42. We believe that further observations of its central star will help develop a better stellar classification and also shed light on the mechanism producing its FLIERs.

A.D. acknowledges the award of a Research Excellence Scholarship from Macquarie University. Q.A.P. acknowledges support from Macquarie University and the Australian Astronomical Observatory (AAO). W.S. acknowledges support from grant UNAM-PAPIIT 101014. We would like to thank the staff at the ANU Siding Spring Observatory for their support. We acknowledge use of data from the VISTA telescope under ESO Survey programme ID 179.B-2002. We thank the anonymous referee whose suggestions and comments have greatly improved the paper.

REFERENCES

Acker, A. & Neiner, C. 2003, A&A, 403, 659
Acker, A., Raytchev, B., Koeppen, J., & Stenholm, B. 1991, A&AS, 89, 237
Akras, S. & López, J. A. 2012, MNRAS, 425, 2197
Balick, B., Alexander, J., Hajian, A. R., Terzian, Y., Perinotto, M., & Patriarchi, P. 1998, AJ, 116, 360
Balick, B., Perinotto, M., Maccioni, A., Terzian, Y., & Hajian, A. 1994, ApJ, 424, 800
Balick, B., Rugers, M., Terzian, Y., & Chengalur, J. N. 1993, ApJ, 411, 778
Cahn, J. H., Kaler, J. B., & Stanghellini, L. 1992, A&AS, 94, 399
Crowther, P. A., De Marco, O., & Barlow, M. J. 1998, MNRAS, 296, 367
Danehkar, A. 2014, PhD thesis, Macquarie University
Danehkar, A. & Parker, Q. A. 2015, MNRAS, 449, L56
Danehkar, A. & Parker, Q. A. 2016, in IAU Symp. 312, Star Clusters and Black Holes in Galaxies Across Cosmic Time, ed. Spurzem, R. and Liu, F. and Li, S. and Meiron, Y., arXiv:1412.0012
Danehkar, A., Parker, Q. A., & Ercolano, B. 2013, MNRAS, 434, 1513
Danehkar, A., Todt, H., Ercolano, B., & Kniazev, A. Y. 2014, MNRAS, 439, 3605
DePew, K., Parker, Q. A., Miszalski, B., De Marco, O., Frew, D. J., Acker, A., Kovacevic, A. V., & Sharp, R. G. 2011, MNRAS, 414, 2812
Dopita, M., Hart, J., McGregor, P., Oates, P., Bloxham, G., & Jones, D. 2007, Ap&SS, 310, 255
Dopita, M., Rhee, J., Farage, C., McGregor, P., Bloxham, G., Green, A., Roberts, B., Neilson, J., Wilson, G., Young, P., Firth, P., Busarello, G., & Merluzzi, P. 2010, Ap&SS, 327, 245
Dopita, M. A. & Meatheringham, S. J. 1990, ApJ, 357, 140
—. 1991, ApJ, 377, 480
Durand, S., Acker, A., & Zijlstra, A. 1998, A&AS, 132, 13
Falceta-Gonçalves, D. & Monteiro, H. 2014, MNRAS, 438, 2853
Frew, D. J., Bojičić, I. S., & Parker, Q. A. 2013, MNRAS, 431, 2
Frew, D. J., Parker, Q. A., & Bojičić, I. S. 2016, MNRAS, 455, 1459
García-Díaz, M. T., López, J. A., Steffen, W., & Richer, M. G. 2012, ApJ, 761, 172
Gómez-Muñoz, M. A., Blanco Cárdenas, M. W., Vázquez, R., Zavala, S., Guillén, P. F., & Ayala, S. 2015, MNRAS, 453, 4175
Gonçalves, D. R., Corradi, R. L. M., Mampaso, A., & Perinotto, M. 2003, ApJ, 597, 975
Gonçalves, D. R., Ercolano, B., Carnero, A., Mampaso, A., & Corradi, R. L. M. 2006, MNRAS, 365, 1039
Howarth, I. D. & Adams, S. 1981, Program EQUIB, University College London, (Wesson R., 2009, Converted to FORTRAN 90)
Kingsburgh, R. L. & Barlow, M. J. 1994, MNRAS, 271, 257
Liu, X.-W., Storey, P. J., Barlow, M. J., Danziger, I. J., Cohen, M., & Bryce, M. 2000, MNRAS, 312, 585
López, J. A., Richer, M. G., García-Díaz, M. T., Clark, D. M., Meaburn, J., Riesgo, H., Steffen, W., & Lloyd, M. 2012, RMxAA, 48, 3
Minkowski, R. 1947, PASP, 59, 257
Nordhaus, J. & Blackman, E. G. 2006, MNRAS, 370, 2004
Parker, Q. A., Phillipps, S., Pierce, M., & et al. 2005, MNRAS, 362, 689
Preite-Martinez, A., Acker, A., Koeppen, J., & Stenholm, B. 1989, A&AS, 81, 309
Rees, B. & Zijlstra, A. A. 2013, MNRAS, 435, 975
Reid, W. A. & Parker, Q. A. 2010, Publ. Astron. Soc. Australia, 27, 187
Saito, R. K., Hempel, M., Minniti, D., & et al. 2012, A&A, 537, A107
Stanghellini, L., Shaw, R. A., & Villaver, E. 2008, ApJ, 689, 194
Steffen, W., García-Segura, G., & Koning, N. 2009, ApJ, 691, 696
Steffen, W., Koning, N., Wenger, S., Morisset, C., & Magnor, M. 2011, IEEE Trans. Vis. Comput. Graphics, 17, 454
Steffen, W. & López, J. A. 2006, RMxAA, 42, 99
Tylenda, R., Acker, A., Raytchev, B., Stenholm, B., & Gleizes, F. 1991a, A&AS, 89, 77
Tylenda, R., Acker, A., & Stenholm, B. 1993, A&AS, 102, 595
Tylenda, R., Stasińska, G., Acker, A., & Stenholm, B. 1991b, A&A, 246, 221
van der Hucht, K. A. 2001, New Astro. Rev., 45, 135
Wang, W. & Liu, X.-W. 2007, MNRAS, 381, 669
Wareing, C. J., Zijlstra, A. A., & O'Brien, T. J. 2007, MNRAS, 382, 1233